CLAS-NOTE 2011-005

TOF Resolution Measurements with the CLAS12 Central TOF Detector with Fine-Mesh Photomultiplier Tubes

V. Baturin, S. Boiarinov, V. Burkert, D.S. Carman,
L. Elouadrhiri, D. Kashy, E. Pasyuk,
S. Pozdniakov, A. Reusle, A. Selvaratnam, I. Strakovsky

April 1, 2011

Abstract

The CLAS12 detector is being constructed at JLab and one of its detector components, the Central Time-Of-Flight barrel, is being tested for a final choice of its PMT design. We report on the comparative time-of-flight resolution measurements with prototype CTOF counters utilizing Hamamatsu R5924 fine-mesh PMTs and conventional linear-focused Hamamatsu R2083 PMTs.

Contents

1 Introduction

The timing information in the CLAS12 Central Time-of-Flight (CTOF) detector, shown in Fig. 1, will be referenced to a stable radio-frequency signal from the accelerator. Due to the double-sided readout of the scintillators, the corresponding time-of-flight (TOF) is given by:

$$TOF = \frac{1}{2}(t_l + t_r), \tag{1}$$

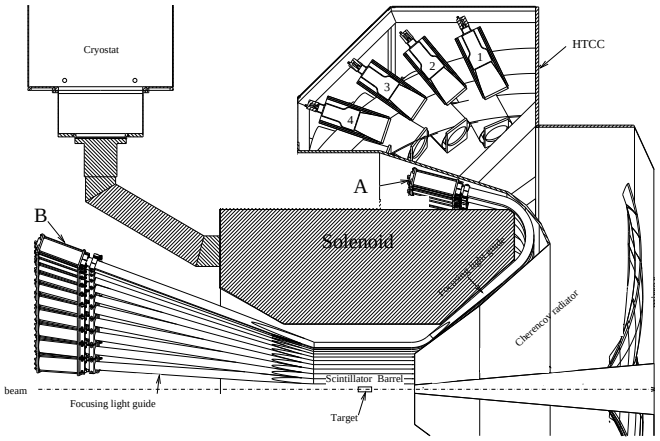

Figure 1: Cut view of the top half of the CTOF detector. A: - downstream readout PMTs, B: - upstream readout PMTs, 1-4: - PMTs of the High Threshold Cherenkov Counter (HTCC).

where t_l and t_r are the TDC-digitized intervals between the discriminated PMT "start"-signals and the common "stop"-signal, generated by the CLAS12 trigger in coincidence with the RF-oscillator of the accelerator. Assuming that the two PMTs are identical, the TOF resolution may be determined as[1]:

$$\sigma_{TOF} = \frac{1}{\sqrt{2}}\,\sigma_{pm}, \tag{2}$$

where σ_{pm} is the effective time resolution of the PMT.

Physics requirements. The physics requirements of the CTOF detector are based on the simulated TOF distributions of incident secondary pions, kaons, and protons at 90° (lab system) shown in Fig. 2. The ultimate requirement is to guarantee a 3.3-σ (standard deviation) separation of protons from pions up to 1.25 GeV/c and pions from kaons up to 0.64 GeV/c. Provided that the TOF resolution is at least 60 ps, this implies a 200 ps separation at the particle momenta indicated in Fig. 2. Thus our goal is a CTOF time-of-flight resolution of:

$$\sigma_{TOF} \leq 60 \text{ ps}. \tag{3}$$

This is equivalent to an effective PMT resolution of $\sigma_{pm} \leq 84$ ps.

[1]We neglect any possible correlations between the two signals.

Particle misidentification and TOF resolution. The TOF measurement is not an end in itself as it will be used for particle identification. Due to the Gaussian nature of the TOF distributions at fixed momenta[2], the identification of particles is subject to probability. The probability of misidentification is proportional to the background of foreign particles under the main TOF peak that follows a Gaussian distribution. Table 1 shows how the performance of the CTOF detector depends on σ_{TOF}.

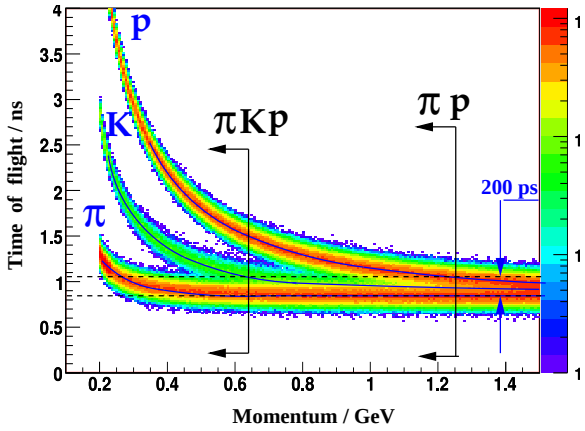

Figure 2: Monte Carlo simulations of particle time of flight vs. momentum for pions, kaons, and protons emitted at 90° in the laboratory frame.

σ_{TOF}	r=200 ps/σ_{TOF}	exp($-r^2/2$)	Bkg Factor
60 ps	3.33	0.004	1.0
66 ps	3.03	0.010	2.5
90 ps	2.22	0.085	21.3

Table 1: TOF resolution and foreign particle background at 200 ps separation.

In the first column of this table the CTOF timing resolution is listed. In the second column we estimate the ratio of the separation time interval to the TOF resolution. Here, in the first row this ratio corresponds to the nominal separation in terms of standard deviations. In the third column the exponential factor of the Gaussian is listed. From the last column one may get a feeling for how the background changes with the TOF resolution. From this column we can see that for only a 10% worsen TOF-resolution, more than double the background of foreign particles is present, while a 50% worse resolution results in more than 20 times higher backgrounds.

Thus, even a 10% improvement in the TOF resolution will result in a factor of 2.5 times lower number of misidentified particles. Therefore, the effective PMT resolution should be improved by all possible means.

[2]A momentum slice of the scatterplot in Fig. 2.

Effective rise time of the PMT output signal. We refer to σ_{pm} as an "effective resolution" of a PMT since it is determined not only by the intrinsic characteristics of the PMTs, such as the transition time spread (TTS) and the signal rise time (τ_{pm}), but to an even greater degree it depends on the scintillator rise time (τ_{sc}), the light propagation time spread (τ_{pr}), the feeder system rise time (τ_{fd}), and the discriminator design and threshold. All of these timing parameters are combined into an effective rise time (τ) of signals from the PMT that can be observed via an oscilloscope[3] as:

$$\tau^2 = \tau_{pm}^2 + \tau_{sc}^2 + \tau_{pr}^2 + \tau_{fd}^2. \tag{4}$$

We can compare the τ-values for the Hamamatsu R5924 and R2083 PMTs using Eq.(4) and reasonable estimates for τ_{sc} and τ_{pr}, neglecting τ_{fd} for the feeder system. The rise time of BC-408 scintillator is 0.8 ns. The maximum propagation time spread of primary photons is determined by the longest and shortest trajectories, i.e. by the difference between the trajectory corresponding to the total internal reflection (TIR) angle and the path along the scintillator axis, respectively:

$$\tau_{pr} = l\left(\cos^{-1}(\theta) - 1\right)\frac{n}{c} \quad , \quad \theta = \alpha, \tag{5}$$

where θ is the angle between the photon direction and the axis of the guiding system, α is the angle of total internal reflection, l is the length of the light guiding system, n is the refractive index of the light guiding media, and c is the speed of light in vacuum.

For a 1-m-long light guiding system, from Eq.(5) we find that:

$$\tau_{max} \approx 2 \text{ ns}. \tag{6}$$

For a uniform distribution of x, y, and z-components of the photon velocity, the mean value of τ_{pr} within the interval $0 \leq \theta \leq \alpha$ can be computed analytically from Eq.(5) as:

$$\tau_m \approx \frac{1}{3} l \frac{n}{c} \approx 1.5 \text{ ns}. \tag{7}$$

Using τ_m in place of τ_{pr} in Eq.(4), with the 1-m-long light guide to the photocathode of the R2083 PMT, we find

$$\tau_{R2083} \approx \sqrt{0.7^2 + 0.8^2 + 1.5^2} \text{ ns} \approx 1.8 \text{ ns}, \tag{8}$$

while for the same guiding system to the R5924 PMT we find

$$\tau_{R5924} \approx \sqrt{2.6^2 + 0.8^2 + 1.5^2} \text{ ns} \approx 3.1 \text{ ns}. \tag{9}$$

Signal rise time and effective time resolution resolution of PMTs. Typically a signal from the PMT is fed to a discriminator that forms a logic signal, which is used to measure the timing of the PMT signal. Whatever the design of the discriminator, at the final stage it compares the current signal generated by the PMT with some predetermined

[3]Not accounting for the feeder and oscilloscope rise times.

threshold. The only parameter that links signal fluctuations, scaled in Volts (V), to the timing, scaled in nanoseconds (ns), is the signal rise time, scaled in V/ns:

$$\frac{dA}{dt} \propto \frac{A}{\tau} \ , \tag{10}$$

where τ is the effective PMT signal rise time (Eq.(4)) and A is the PMT signal amplitude. Thus, the timing fluctuation δt may be determined as:

$$\delta t = \tau \times \frac{\delta A}{A}, \tag{11}$$

where t is the discriminator timing and δA is the statistical fluctuation of the PMT signal. In the statistical limit the following relation holds:

$$\frac{\delta A}{A} \propto \frac{1}{\sqrt{N_{ppe}}}, \tag{12}$$

where N_{ppe} may be considered as the average number of primary photoelectrons; here it is obvious that $A \propto N_{ppe}$. Therefore, one can write

$$\sigma_{pm} \propto \frac{\tau}{\sqrt{N_{ppe}}}. \tag{13}$$

In the above formulas we have neglected the transition time spread (TTS) of the phototube. For the phototubes of interest, such as the Hamamatsu R2083 and R5924 PMTs, the TTS is roughly 400 ps (FWHM). Provided that the typical number of primary photoelectrons is about 400, from Eq.(13) we find that the corresponding timing resolution is:

$$\sigma_{TTS} \leq 10 \text{ ps}. \tag{14}$$

Here, this value would combine into Eq.(13) in quadrature. Therefore, the effects of TTS in our further consideration will be neglected.

Light guide transmittance and effective PMT resolution. The number of primary photoelectrons is the most decisive parameter of the problem. It is determined by several factors, such as the number of photons produced in the scintillator (N_{ph}), the transmittance of the optical system (T), and the quantum efficiency of the photocathode (ϵ) as:

$$N_{ppe} = \epsilon \times T \times N_{ph}. \tag{15}$$

Hence, from Eqs.(12) and (15) we find:

$$\sigma_{pm} \propto \frac{\tau}{\sqrt{T}}. \tag{16}$$

This relation will be widely used in our further estimates.

As seen from Eqs.(13) and (15), in order to achieve the best possible timing resolution, provided the scintillator material and dimensions are predetermined, one has to minimize the signal rise time and maximize the number of primary photoelectrons, i.e. the transmittance of the light guides. These two requirements require that the light guides should be as short

as possible with the highest possible transmittance and that the PMTs should be as fast as possible. First of all, the transmittance of the light guide is a function of its material properties, such as refractive index, bulk attenuation length, and surface reflectivity. Secondly, the light guide transmittance depends on its geometrical shape and size. In particular, the ratio of the light guide entry area[4], S_i, to its exit area[5], S_o, is of crucial importance, since the phase space theorem dictates that the transmittance, T, of the guiding system follows from the relation:

$$T \leq \frac{S_o}{S_i}. \tag{17}$$

Thus, in order to avoid this fundamental limitation, the PMT photocathode area, S_{pc}, has to be larger than the exit area of the scintillator, i.e. in our case we require

$$S_{pc} \geq 10.6 \text{ cm}^2. \tag{18}$$

Below we consider the potential benefits of two alternatives for the CTOF PMTs taking into account the PMT rise time and sensitive areas and parameters of the light guides.

1.1 CTOF Design and PMT Properties

CTOF and timing properties of PMTs. The baseline solution for the CTOF detector makes use of the best timing photomultipliers R2083 from Hamamatsu. The rise time of this PMT is 0.7 ns. It is as short as the scintillation rise time (0.8 ns) of the fast BC-408 scintillator. Unfortunately, these phototubes require long light guides and heavy magnetic shields for use in the CLAS12 detector. Sophisticated focusing light guides (FLG) and dynamical magnetic shields (DMS) were designed with the purpose to retain the excellent timing properties of the R2083 PMT in the fringe fields of the CLAS12 Central Solenoid [1].

In order to avoid heavy magnetic shielding and to halve the length of the light guides, we pursue an option of using fine-mesh Hamamatsu R5924 phototubes, which may operate at very high magnetic fields up to 1 T. Unfortunately, this phototube is 3.5 times slower than the R2083. Its rise time is 2.6 ns.

CTOF and PMT area. Our ultimate goal for the CTOF is a time resolution of 84 ps per PMT. According to Eq.(3), this corresponds to σ_{TOF}=60 ps. It is obvious from Eq.(13) that the signal rise time should be as fast as possible, which is why we use the best timing R2083 PMT. The propagation time of light from the scintillation point to the photocathode has to be minimized, as well as the other values in Eq.(4). That implies that the light guides should be as short as possible.

In the baseline CTOF design with R2083 PMTs, the length of the 1.5-m-long light guides is determined by the fringe magnetic field of the CLAS12 Central Solenoid that can be tolerated by the PMT magnetic shield. However, the optional R5924 fine-mesh PMTs may operate up to 0.8 T. In the environment of the CLAS12 Central Solenoid this requirement implies that the light guides should be roughly 0.8 m long.

[4]The same as the output area of the scintillator.

[5]Typically the output area of light guide matches to the PMT photocathode.

As seen from Eq.(13), the drawback of a very long rise time may be compensated, in principle, by a significantly higher number of primary photoelectrons. Hence, we formulate the question to respond experimentally. Is it possible to compensate the effect of 3.5 times longer rise time by a higher number of primary photoelectrons, implementing fine-mesh PMTs with shorter light guides? Prior to the experimental studies in the next section, we attempt to respond to the main question using simple estimates.

1.2 Light Guide Design and Transmittance

We have optimized the light guide design for both PMT options using the Guide-7 program [2]. This program simulates photon propagation through the sequence of scintillator, light guide, and PMT entry window.

For both linear-focused and fine-mesh PMTs, light guides with a so-called "focusing design" were implemented. In such a design, the cross section of the light guide matches to the scintillator cross section at the scintillator end. At the PMT it fits into the photocathode of the PMT. The shape of such a light guide gradually transforms from a truncated pyramid with a trapezoidal cross section at the entry, to a cylinder in the middle part of the light guide, then to a truncated cone that fits by its narrow part into the PMT area.

Light guides for R2083. For the case of the R2083 PMT, with its 20.4 cm^2 area, the cross section of the focusing light guide almost doubles towards the PMT photocathode. According to the phase space theorem, the angular acceptance doubles, as well. As was previously shown with both Monte Carlo calculations and measurements [3], this feature about doubles the transmittance of focusing light guides compared to a constant cross section.

A substantial improvement in the transmittance was achieved after considering the geometry of the PMT photocathode. Typically, the external photocathode surface is flat. However, the inner photocathode surface of most timing PMTs is a part of a sphere with a radius of 2-3 cm. Due to this shape, the thickness of the PMT entry window varies from 1 mm in the center to 7 mm at the periphery[6]. Thus, the geometry of the PMT entry window should be taken into account, since photons may escape through the periphery of the glass window, and, according to our Monte Carlo simulations, the PMT window effect may reduce the number of primary photoelectrons by up to 30%.

In order to compensate this detrimental effect, the light guides are supplied with a focusing cone at the PMT end. The focusing cone slightly increases the photon angle at the exit. Simultaneously, the cone shrinks the luminous area and provides for slightly better conditions for targeting at the PMT. Since most of photons at the end of the cylindrical part of the light guide propagate within the TIR-angle, the focusing cone directs a substantial fraction of the escaping photons to the spherical photocathode.

The cone generatrix was optimized for the best possible transmittance using various Monte Carlo models of the light guide. An example of the Guide-7 simulations is shown in Fig. 3. The image of the R2083 photocathode with a diffuse border may be seen in this figure. This figure also shows a 2 ns rise time of the light signal at the light guide exit, in agreement with our estimates.

[6]These numbers are given for the R2083 PMT.

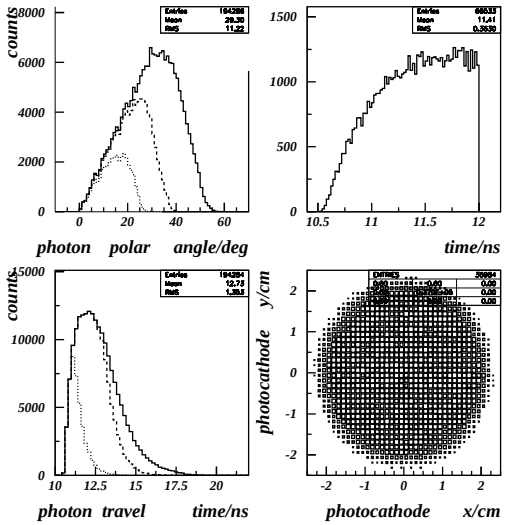

Figure 3: Monte Carlo simulations of light guides. (Top-left). Angular distribution for "fast" (entry pitch below 20°, dotted line), "medium" (entry pitch below 30°, dashed line) and "slow" (entry pitch below 40°, solid line) photons at the exit of the light guide. (Bottom-left). Arrival time distribution for "fast", "medium", and "slow" photons. (Top-right). Arrival time distribution for "fast" photons within the first 1.5 ns. (Bottom-right). Photon hit distribution over the PMT photocathode.

Light guides for R5924. Light guides for fine-mesh PMTs, such as the Hamamatsu R5924, may be about two times shorter. This factor works in favor of higher N_{ppe}, thus, to a better timing resolution. However, the sensitive area of the R5924 is about 40% smaller than that of the R2083. According to the space phase conservation theorem, the smaller the exit area, the wider the angular distribution of the exiting photons should be. Therefore, we expect longer travel distances and a higher number of reflections from the guiding surfaces. The transmittance will be correspondingly lower.

We have performed numerous Monte Carlo simulations of light propagation through focusing light guides for different PMTs. There are two critical parameters for such calculations: the bulk attenuation length of the light guide material and the reflectivity of the guiding surfaces. The bulk attenuation length was measured using a simple setup of a laser and a radiometer [4]. The surface reflectivity was calibrated to the similarly measured transmittance [4] of a reference 1.4-m-long cylinder made of the same material. Some relevant examples of such calculations are summarized in Table 2.

In columns 1 and 2 of this table, the name of the PMT model and its sensitive area are listed. In columns 3 and 4 we show the light guide entry area and the light guide sizes, respectively. Since the light guides are supposed to be fabricated from plastic rods, we show the diameter of such a rod in column 5. The last two columns, 6 and 7, contain two estimates for the light guide transmittance. The estimate in column 6 is the ratio of the number of photons arriving at the photocathode within a 40 ns-interval to the total number of photons that escaped from the scintillator. The second estimate, given in column 7, is more relevant to the signal timing. The ratio in column 7 is given for a train of "fast" photons that arrive

PMT	PMT area/cm^2	LG entry area/cm^2	LG sizes/cm	LG-cyl. OD/mm	Transm. $t_{ph} < 40$ ns	Transm. $t_{ph} < 5$ ns
R2083	16.6	10.6	3×3×150	50.8	0.53	0.32
R5924	11.9	-	3×3×70	-	0.58	0.42
R7761	5.7	-	3×3×70	46.8	0.33	0.25

Table 2: Transmittance of a counter with different light guides. The light is guided first through a pyramid at the scintillator end, and then runs through a cylinder with a focusing cone at the PMT end.

at the photocathode within the first 5 ns. From this table we conclude that the maximum gain in the transmittance for "fast" photons to the R5924 photocathode is about 30%, i.e.

$$T_{R5924} \leq \frac{42}{32} \times T_{R2083} = 1.3 \times T_{R2083}. \tag{19}$$

Now we have enough data to determine the expected relationship between the timing resolutions of the two PMTs. From Eqs.(8), (9), and (19) we find:

$$\sigma_{R5924} \geq \frac{\tau_{R5924}}{\tau_{R2083}} \sqrt{\frac{T_{R2083}}{T_{R5924}}} \times \sigma_{R2083} \approx 1.5\sigma_{R2083}. \tag{20}$$

At first sight the difference is not crucial. However, according to Table 1, a 1.5 times worse time resolution translates to about 20 times higher background levels of foreign particles under the main particle TOF peak.

The last resource to improve the performance of the R5924 PMT could be a super bi-alkali photocathode. Such a photocathode has about 30% higher quantum efficiency in the relevant wavelength domain. Unfortunately, at the current time, Hamamatsu does not plan to implement SBA-technology into fine-mesh PMTs. In addition, due to the wavelength shift between the scintillator and the SBA photocathodes, the time resolution may be improved by only 15-20%, while the cost increase will be about 50% compared to the standard R5924 PMT.

We note that according to Eq.(19) and Table 2, a cheaper R7761 PMT[7] fine-mesh PMT will have a 30% worse time resolution compared to a R5924 PMT and about 80% worse time resolution compared to a R2083. In addition, this PMT has 20 times (!) lower anode current than the baseline R2083 PMT (200 μA) and 10 times lower anode current than a R5924 PMT[8]. Therefore, we do not consider the R7761 PMT as an option for the CTOF detector.

Concluding remarks. The maximum potential benefit in N_{ppe} from the shorter focusing light guides for the R5924 phototubes is about 30%. The effect of shorter propagation distances in light guides of half the nominal CTOF length was accounted for by Eqs.(8) and (9). From these equations we find that due to a longer rise time of the R5924, its timing

[7]Its photocathode area is 3 times smaller than the R2083 and 2.1 times smaller than the R5924.

[8]From our Geant-3 simulation, the expected PMT current is 60 μA.

resolution will be at least 50% worse than that of the R2083. However, the question of whether or not a shorter light guide would help to compensate the 3.5 times slower response of the R5924 PMT should be investigated experimentally.

2 CTOF Prototype Counter with Fine-Mesh PMTs

The timing resolution measurements we report in this note were performed with a prototype CTOF counter with fine-mesh PMTs (called the CTOF-FM prototype). The scintillator is a 66-cm-long BC-404 bar of trapezoidal cross section with a 10.6 cm^2 luminous area. Two PMTs are coupled to the scintillator via 0.85-m-long light guides. The design of all elements of this counter, including the light guides, fits into a 7.2° sector, i.e. 1/50 of the full CTOF barrel. The drawing of this detector is shown in Fig. 4 together with the readout circuit diagram.

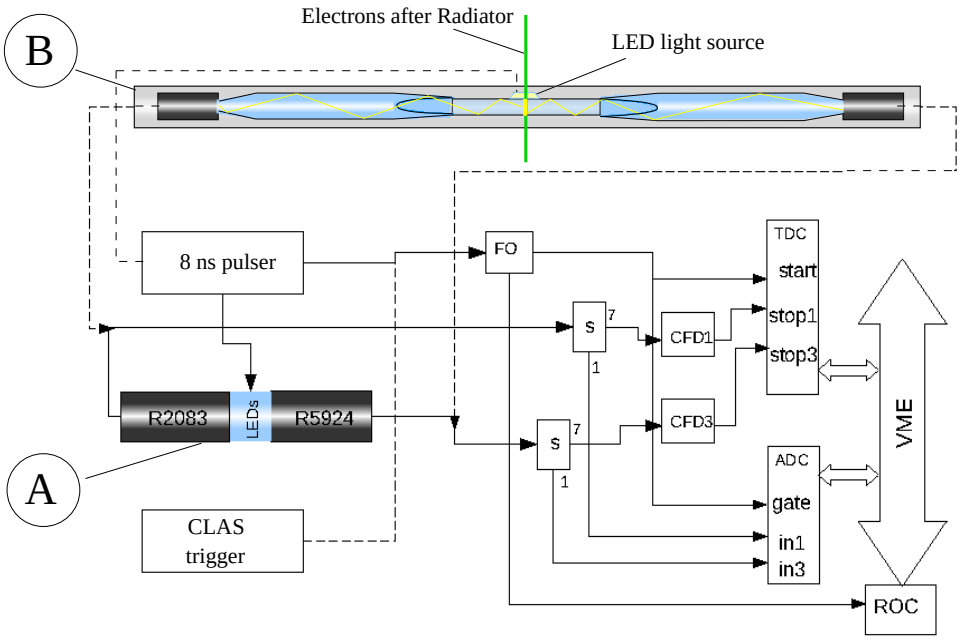

Figure 4: The layout of the CTOF-FM prototype together with the readout circuit diagram for the LED tests (not to scale). Two different PMT setups were used for the bench (A) and beam (B) tests, respectively. The readout configuration for the beam tests is shown with the dashed lines.

The comparative resolution tests of PMT candidates were performed using the simple setup "A" shown in Fig. 4. This setup is comprised of two PMTs undergoing resolution tests and a fast LED light source. The light source is a Teflon washer with four blue LEDs inserted through radial holes. Thus, the LEDs emit light to the center of the Teflon piece. With a 1 GHz oscilloscope, the R2083 anode signal rise time was adjusted to 2 ns, which is what is expected for the CTOF scintillators.

The timing resolution of the CTOF counter was first studied on the test bench with setup "B" shown in Fig. 4. With this goal in mind, the LED light source was placed in the middle of the counter (see Fig. 4). This light source was comprised of two LEDs inserted into an acrylic prism. The LEDs emit light at 40° to the scintillator axis. The optical contact between the acrylic prism and the scintillator was provided with optical grease. This allowed us to inject the LED-light into the scintillator at 40° to its axis without reflections.

For the TOF resolution measurements in a beam of minimum ionizing particles (MIPs), the CTOF counter (setup "B", Fig. 4) was placed in the Tagger Alcove in Hall B. The main electron beam of Hall B hits the photon radiator resulting in photons from the secondary photon beam that had been used for the main studies with CLAS. Scattered electrons were bent by the Tagger magnet and then registered by the hodoscope of 384 scintillation counters (Hall B Tagger). The CTOF-FM counter was placed beneath the Tagger hodoscope. Thus, its signal coincided with certain Tagger counters. The details of the assembly and the measuring method are given in Sections 3, 4, and 5.2.

2.1 Counter Preparation

Scintillator. The scintillator is 66-cm-long BC-404 with a geometry such that it is a precise 1/50 portion of a barrel. Therefore, it has a trapezoidal cross section $\approx 3 \times 3$ cm^2. The light output area of the scintillator is 10.6 cm^2. The scintillator is coupled to the light guides with the same cross section at its entry via optical grease.

Wrapping. The scintillator and the light guides are wrapped with enhanced reflective material VM2002 [9]. Opaque wrapping was not used since the counter was placed inside a 3-m-long aluminum pipe. The light tightness of the inner volume was ensured with rubber foam boots.

Photomultipliers. Our main reference PMT is the Hamamatsu R2083. Actually we used the H2431 assembly of this PMT with a magnetic shield made of 0.8-mm-thick μ-metal. This element works as both a magnetic shield and an electromagnetic shield against high frequency radiation.

The R5924 fine-mesh PMTs do not require a magnetic shield. However, the electromagnetic shield is an obligatory part, without which reliable measurements are not possible. Therefore, the fine-mesh PMTs were enclosed into an aluminum case which, by its design, is similar to the metal case for the R2083 phototube in the H2431 assembly.

Counter Assembly. For flexibility we did not glue the light guides to the scintillators. The two PMTs, two light guides, and the scintillator were assembled inside the aluminum tube that works, simultaneously, as a holding structure for all axial elements, as a light-tight case, and as additional electromagnetic shielding. All elements of the counter were equipped with "piston-rings" that provided the overall coaxiality inside the pipe. The PMT assemblies were pressed to the ends of the light guides via a stainless steel spring. The springs were held by three studs mounted at one side of the pipe through radial holes. At the opposite

[9] A super-radiant mirror film from the 3M Company.

side, the assembly was held by a stationary plastic ring mounted on the inner side of the pipe.

Optical grease was spread over the PMT window and the assembly had been pressed with a force of 1-2 lbs. Hence, reliable and stable optical contact was provided during the measurements.

The main advantage of such a design is that it allows quick replacement (within only a few minutes) of any counter element, for example one or two PMTs or even light guides. This proved to be very useful.

2.2 Readout Electronics and Logic

Signals from the PMT anodes were, at first, routed to the passive 1:5 splitter (see Fig. 4) via 15-m long cables, and then to an ORTEC 935 constant fraction discriminator (CFD). The external signal from the CLAS detector was used to form the readout trigger during the electron beam tests (dashed lines in Fig. 4).

Bench tests. For the test bench measurements the trigger had been taken from the pulse generator that controlled the LED-light source. The common TDC start and the QDC gate were generated by a LeCroy 465 coincidence unit in response to the signals from the pulser. A 200-ns-long NIM signal was routed to the "common start" input of a CAEN V792 TDC (with a 35 ps LSB) and to the "gate" input of a 25 fC CAEN V775 QDC.

The high voltages were fed to the R2083 PMTs by a CAEN A734N power supply operating under SY527 control. The fine-mesh PMTs were fed with positive high voltage using an ORTEC power supply.

Beam tests. For the beam measurements the external trigger was taken from the main CLAS detector. The common TDC start and the QDC gate were generated by the CLAS trigger system in response to a valid combination of CLAS signals. The start signal from CLAS was routed to the "common start" input of a CAEN V1290N TDC (LSB 25 ps) and to the "gate" input of a 50 fC FASTBUS QDC. The high voltages were fed to both PMTs by a LeCroy power supply operating under remote control.

3 Measuring Method

The measurements for the CTOF-FM counter were performed with different methods and installations. Presenting the results in terms of the resolution per PMT (σ_{PMT}), allows comparison of the various prototyping configurations. The TOF resolution may be then estimated from σ_{PMT} using corresponding formulas.

In general, the CTOF will measure particle time-of-flight relative to the very stable and accurate[10] radio frequency signal of the accelerator. For both readout PMTs the signal times $t_{1,2}$ and amplitudes $q_{1,2}$ are digitized.

[10]Better than 2 ps.

3.1 Particle Coordinate Along Counter

Although the main function of the CTOF is to measure timing information, it will also provide a measure of the hit coordinate x_t along the scintillators. In the linear approximation this coordinate is given by:

$$x_t = \frac{1}{2v}(t_1 - t_2) + c_x, \tag{21}$$

where t_1 and t_2 are the hit times from the two PMTs, v is the effective speed of light in the scintillator[11], and c_x calibrates x_t to zero in the middle of the counter. Here we note that the PMT timing values t_1 and t_2 are digitized by different TDC channels between corresponding PMT signals and a common "stop", referenced to the RF of the accelerator or to the LED pulser.

We also determine additional, independent particle coordinates x_s using the QDC information. The following relation has been used:

$$x_q = \frac{L_a}{2} \ln\left(\frac{q_1}{q_2}\right) + c_q, \tag{22}$$

where L_a is the scintillator attenuation length, q_1 and q_2 are the pedestal subtracted and properly calibrated QDC values from the two PMTs, and c_q calibrates x_q to zero in the middle of the counter. This relation was obtained under the assumption of an exponential dependence:

$$q_i = a_i \exp\left(-\frac{x_t}{L_a}\right), \tag{23}$$

where a_i at $i = 1, 2$ are the calibrating factors to provide $q_1 = q_2$ in the center of the counter and x_t is the hit coordinate from Eq.(21). The attenuation length has been determined from the experimental x_t-dependence of the average signal amplitude evaluated from the scatterplots of q_i vs. x_t using several slices of the hit coordinate x_t.

3.2 Time-of-Flight in CLAS12

The moment of the light flash in the scintillator, i.e. the particle time-of-flight, has been determined as:

$$t_{TOF} = \frac{1}{2}(t_1 + t_2) - t_{RF}, \tag{24}$$

where t_{tof} is the TOF value, t_1 and t_2 are the properly calibrated time moments from the two PMTs, and t_{RF} is the properly calibrated timing of the accelerator radio frequency signal. In a first approximation, the determined TOF value does not depend on the particle coordinates. For the bench test, the RF signal has been replaced by a very stable NIM output signal of the LED pulser.

[11] It is roughly 15-16 cm/ns.

3.3 Number of Primary Photoelectrons

We assume that the signal charge measured by the QDC, q_i, is proportional to the number of photoelectrons, N_i, emitted by the photocathode of ith PMT:

$$q_i = \alpha_i N_i, \qquad var(q_i) = \alpha_i^2 N_i, \tag{25}$$

where α_i is the effective gain of the readout channel $i = 1, 2$, including the PMT gain, and the QDC calibrating constants.

We can consider a scatterplot of events in the plane of new variables q_+ and q_- defined as:

$$q_\pm = \frac{1}{\sqrt{2}}(q_1 \pm q_2). \tag{26}$$

This transformation is equivalent to the rotation at an angle of 45° since the density is conserved due to the Jacobian factor $\frac{1}{\sqrt{2}}$. Thus, we may write:

$$2var(q_\pm) = var(q_1) + var(q_2) \pm 2cov(q_1, q_2). \tag{27}$$

Now consider a slice of the overall statistics that satisfy the following requirement:

$$q_+ = const. \tag{28}$$

According to this equation the covariance of the left side term is zero. From the last condition we find that

$$var(q_1) + var(q_2) = -2cov(q_1, q_2). \tag{29}$$

Substituting this result into $var(q_-)$ defined in Eq.(27), we find that

$$var(q_-) = var(q_1) + var(q_2). \tag{30}$$

Using Eq.(25) and assuming that

$$\alpha_1 = \alpha_2 = \alpha, \tag{31}$$

we can write:

$$var(q_-) = \alpha_1^2 N_1 + \alpha_2^2 N_2 = \alpha^2 (N_1 + N_2). \tag{32}$$

We note that the assumption in Eq.(31) implies that the two readout channels are calibrated to the same value, for example, to the mean charge produced by MIP particles. Now we recall that according to Eqs.(25) and (26)

$$\sqrt{2} q_+ = \alpha_1 N_1 + \alpha_2 N_2 = \alpha (N_1 + N_2). \tag{33}$$

Then, using Eqs.(32) and (33), and assuming Eq.(31), we exclude the unknown coefficient α and evaluate the total number of primary photoelectrons as:

$$N_{ppe} = N_1 + N_2 = \frac{2q_+^2}{var(q_-)}, \tag{34}$$

where both values $q_\pm$ have been determined from the calibrated QDC values on an event-by-event basis.

4 Time Resolution Measurements at Test Bench

Comparative time resolution measurements of different PMTs were performed with setup "A" shown in Fig. 4. One example of such a measurement is shown in Fig. 5.

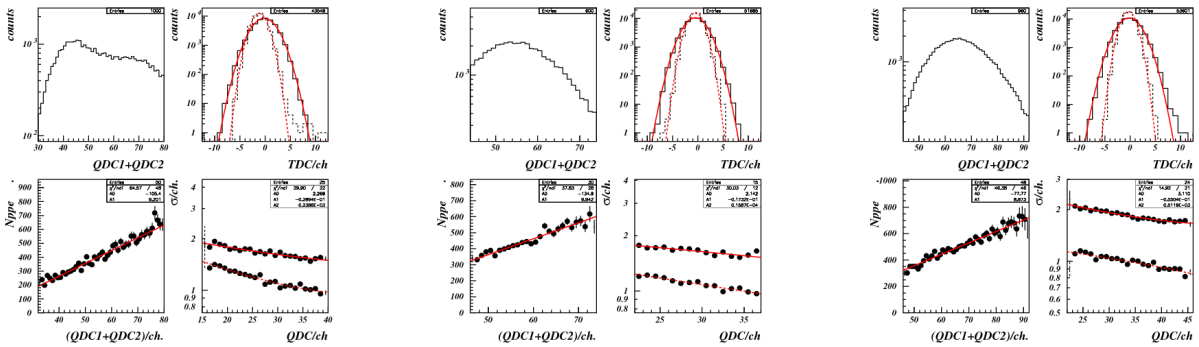

(a) (b) (c)

Figure 5: Comparison of different electromagnetic shielding for R5924 fine-mesh PMTs. Each figure (a), (b), and (c) contains the following plots. (Top-left). $QDC_1 + QDC_2$ distribution. (Top-right). TDC_1 and TDC_2 distributions. (Bottom-left). N_{ppe} as a function of $QDC_1 + QDC_2$. (Bottom-right). Standard deviation of PMT timing as a function of $QDC = (QDC_1 + QDC_2)/2$ for the R5924 (top curve) and R2083 (bottom curve). (a). Brass wrapping around the PMT grounded to the chassis. (b). Brass wrapping grounded to the signal cable braiding. (c). Aluminum shielding case with mounted HV and LV connectors.

Time resolution and electromagnetic shielding. In Fig. 5 we study the effect of electromagnetic shielding on the timing resolution of the R5924. We note that ordinary PMTs, such as the R2083, have been used with magnetic shields, which simultaneously work as a robust electromagnetic shield as well. Fine-mesh PMTs do not require a magnetic shield. However, the electromagnetic shield is not abandoned. Moreover, it is an obligatory part in the environment of the experimental hall, where cross-talk and pickup are an everyday occurrence.

In Fig. 5a and 5b we study the effect of a simple shield. This shield is a flat 0.3-mm-thick brass cylinder grounded to the setup chassis. From this figure we notice that, being a function of $N_{ppe} \propto QDC$, the resolution of the R2083 (bottom curve at the bottom-right panel) follows Eq.(13). However, the resolution of the R5924 (top curve in the same panel)

does not. It is seen in this figure that with a decreasing signal amplitude ($\propto N_{ppe}$), the ratio of σ_{R5924} to σ_{R2083} decreases, and it looks like there is a mechanism that substantially "improves" the resolution of the R5924 compared to R2083 at low signal amplitudes. The very likely reason for this strange phenomenon may be the effect of cross-talk. The cross-talk between different components of the setup very often results in a "fake" resolution that is typically better than the true values.

Resolution and cross-talk. As was already mentioned, the R2083 is enclosed in magnetic shielding[12] that works as a perfect electromagnetic shield, as well. Therefore, this PMT is insensitive to other signals in the setup and that is why its timing resolution follows the statistical law of Eq.(13).

The second PMT, the R5924, was only "wrapped" with a 0.3-mm-thick brass foil that was grounded to the setup chassis via the signal cable braiding. However, both the photocathode and the divider were open for pickup. Thus, the signal of the R5924 could mix with a portion of the LED pulses and/or with the pickup signals from the R2083. In both cases, the timing resolution of the R5924 readout channel may be substantially improved by the admixed signal from the pulser or the more precise R2083 readout channel. It is easy to see that such an effect will be more pronounced at lower amplitudes of the R5924 signals, and we note that the R5924 displays just such a behavior in Fig. 5a.

Resolution and improved electromagnetic shielding. In Fig. 5c we study the R5924 assembly with the PMT-case, similar to that of the R2083 within the H2431 assembly. The only difference is that the μ-metal is replaced with aluminum. As seen from this figure, both phototubes follow Eq.(13). With a robust electromagnetic shield, the timing resolution of the R5924 is about two times worse overall compared to the N_{ppe} domain.

Possible sources of cross-talk. The most likely source for the R5924 pickup is the electromagnetic radiation of the LED assembly. The signal from the R2083 appears in the readout system with a 16 ns delay relative to the LED pulse, while the R5924 signal is delayed by only 10 ns. Note that the difference of 6 ns is equivalent to a 1.2-m difference in cable length, and the effect of the cable length seems to be sensible.

If there are two identical readout PMT channels, such as the R5924, then their cross-talk may be the explanation for "very good" timing resolution, provided that the resolution has been measured with the so-called "coordinate method", where one PMT generates a "start" while another one generates a "stop" signal.

We note that the R5924 typical gain is very high and the signal amplitude may be very high (up to 5-10 V at 50 Ω load), as well. In combination with a "naked" accelerating system and/or divider components, this allows for introduction of cross-talk.

Concluding remarks. We conclude that, firstly, fine-mesh PMTs should not be used without robust electromagnetic shields. Secondly, with robust shielding the timing resolution of R5924 PMTs is about two times worse than that for a R2083 PMT.

[12] We use this PMT in the H2431 assembly.

5 CTOF-FM Resolution Measurements

Our goal is to fabricate the CTOF detector that satisfy the physics requirements from Section 1.

5.1 Test Bench Measurements

5.1.1 Setup and Test Conditions

Bench test measurements of the CTOF counter prototype were performed with setup "B" shown in Fig. 4. The LED light source of this setup was placed between the two PMTs undergoing tests. The signal from the generator was adjusted to the desired signal rise time of 2 ns for the R2083 PMT and 3.6 ns for the R5924 PMT. The amplitude was set to be close to that for MIP particles, i.e. within an interval corresponding to 300-500 primary photoelectrons per PMT. The counting rate varied from 1 Hz to 300 kHz with the same result.

Presumably, the counter design provides an identical average number of primary photoelectrons for either of the two PMTs due to the focusing design of light guides[13].

5.1.2 Comparative PMT Time Resolution Tests

R2083 (left) - R5924 (right). The resulting resolution of the R2083 PMT on the left side in comparison to the simultaneously measured resolution of the R5924 PMT on the right side is shown in Fig. 6a. The resolution of the R5924 is about two times worse in the full N_{ppe} domain. In order to verify the systematics related to the light guide transmittance etc., we swapped the PMTs and repeated the measurements.

R5924 (left) - R2083 (right). After swapping the PMTs, we obtained noticeably different timing resolutions for the two PMTs, as seen in Fig. 6b. Although, the high voltages were increased to double the PMT gains, the total number of photoelectrons did not change. Therefore, the only explanation for this effect is that the transmittance of the left and right light guides are not identical.

Taking into account the aforementioned peculiarities of our first test, for comparison, we use the resolution values obtained in the best conditions. According to Fig. 6a, the resolution of the R2083 at 300 photoelectrons is 74 ps. For the fine-mesh R5924 PMT at the same conditions from Fig. 6b, we read its time resolution value of 140 ps.

Transmittance and wrapping. We attribute the observed pecularity in transmittance of the light guides to the specific properties of VM2002. This material consists of very thin layers of transparent plastic, and its enhanced reflectivity is provided by interference effects. Under strong pressure the air gap between the VM2002 film and the acrylic surface is eliminated. Thus, the reflection condition at the first layer is violated and further layers do not work as well. Hence, even the small pressure applied by electrical tape, creates dead zones with very low reflectivity.

[13]The transmittance of the light guides was optimized for the R5924 using Monte Carlo simulations.

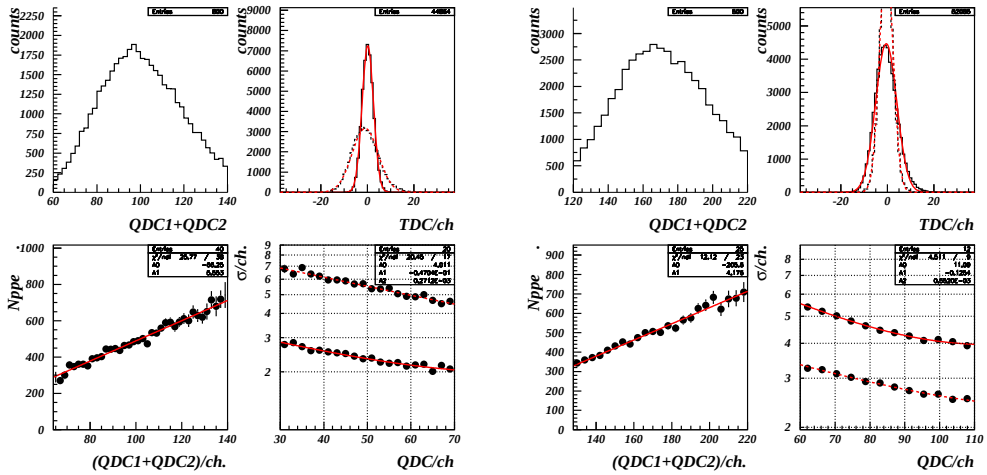

(a) (b)

Figure 6: Comparison of the R2083 PMT at opposite sides of the CTOF-FM counter. (a) Fine-mesh R5924 PMT is on the right side of the counter, while the R2083 PMT is on the left side.(b) The PMTs are swapped. (Top-left). $QDC_1 + QDC_2$ distribution. (Top-right) TDC distribution of the two PMTs. (Bottom-left) N_{ppe} as a function of the QDC values. (Bottom-right) Resolution of the fine-mesh (top curve) and the linear-focused (bottom curve) PMTs as a function of $QDC = (QDC_1 + QDC_2)/2$. The corresponding N_{ppe} distribution for the two photocathodes may be ascertained from the previous panel.

We modified the wrapping scheme to retain an air gap. After this modification the PMT swapping did not affect the measured resolutions.

R5924-R5924. The next step is to determine the time resolution of the CTOF-FM counter with R5924 PMTs at both ends. The results of the LED test with this counter are shown in Figs. 7a and 7b. The bottom-right and bottom-left panels of Fig. 7a show $QDC_1 + QDC_2$ vs. $QDC_1 - QDC_2$ and QDC_1 vs. QDC_2 plots, respectively. These plots show that the QDC spectra of the two readout channels are calibrated to the same value. The top-right scatterplot exhibits no dependence of the PMT_2 timing upon the PMT-signal magnitude, QDC_2. The bottom-left panel contains the plot of N_{ppe} $(QDC_1 + QDC_2)$. This plot was created using the definition for N_{ppe} given by Eq.(34). The denominator for this formula was evaluated from a Gaussian fit of the $QDC_1 - QDC_2$ histogram for each $QDC_1 + QDC_2$-slice of the scatterplot, shown in the top-left panel. Here, the mean value of $QDC_1 + QDC_2$ for a current slice was used as the numerator of Eq.(34). This plot allows us to link the N_{ppe} values to another digitized variable $QDC = (QDC_1 + QDC_2)$ that is used in Fig. 7b.

In the top-left panel of these figures, the $QDC_1 + QDC_2$ histogram is shown. In the top-right panel one can see the TDC distributions for the two PMTs, which are almost identical now. The two bottom panels display two σ_{PMT} dependencies on the previously defined QDC that may be linked to N_{ppe} via the bottom-right plot of Fig. 7a.

From these figures we conclude that the two R5924 PMTs have almost identical timing resolution, following the statistical law in Eq.(13). From the σ_{PMT}-plots, we read that the

mean effective R5924 PMT time resolution at 300 photoelectrons is 3.65 TDC channels, i.e 130 ps, in good agreement with previous data.

Concluding remarks. The tests of the CTOF-FM counter with an LED light source show that the resolution of the R5924 PMT is 1.9 times worse than the R2083 PMT over a wide range of N_{ppe} at varying gains and transmittances.

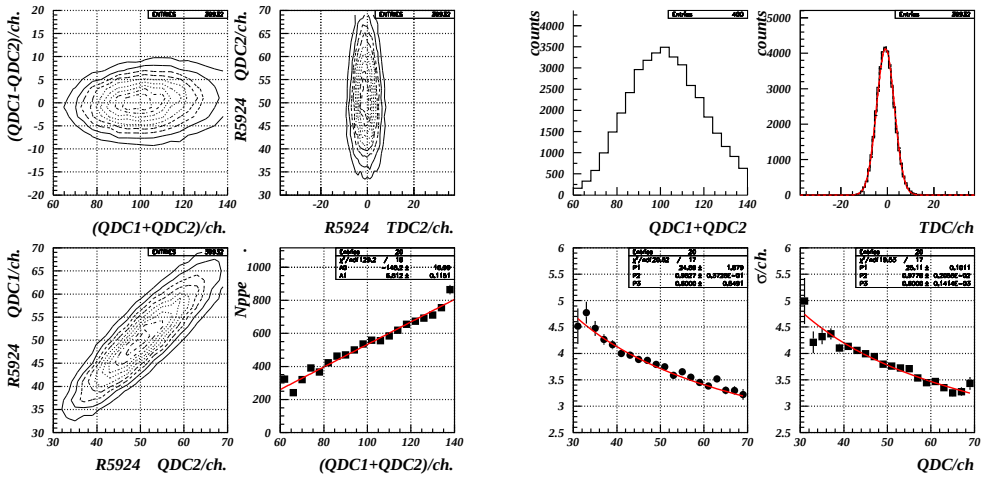

(a) (b)

Figure 7: Time resolution test of the R5924-R5924 counter with an LED light source. (a).Number of primary photoelectrons. (Top-left). $QDC_1 + QDC_2$ vs. $QDC_1 - QDC_2$. (Top-right). TDC vs. QDC of one of the PMTs. (Bottom-left). QDC_1 vs. QDC_2. (Bottom-right). N_{ppe} vs. $QDC_1 + QDC_2$. (b). Time resolution as a function of N_{ppe}. (Top-left). $QDC_1 + QDC_2$ distribution. (Top-right). TDC distributions. (Bottom-left). Time resolution σ_{PMT} of PMT_1 vs. $QDC = (QDC_1 + QDC_2)/2$. (Bottom-right). The same for the right PMT_2.

5.2 Electron Beam Measurements

5.2.1 Measuring Environments

The data were taken with the secondary electrons deflected by the Tagger magnet. The external trigger was taken from the main CLAS detector. The common TDC "stop" and the QDC "gate" were generated by the CLAS trigger system as well, in response to a required combination of CLAS signals. The common signal from CLAS was routed to the "common stop" input of a multi-hit CAEN V1290N TDC (with LSB 25 ps) and to the "gate" input of a 50 fC FASTBUS LeCroy 1881M QDC. The high voltages were fed to both PMTs by a LeCroy power supply operating under remote control.

Substantial time was spent for commissioning and readout optimization. However, we did not succeed to eliminate all sources of noise pickup, because the readout QDC was separated by about 100 m from the detector in a very noisy environment. Therefore, a certain portion

of the pickup fed to the discriminator inputs via the QDC cables. The indication of such effects may be seen in Fig. 8a.

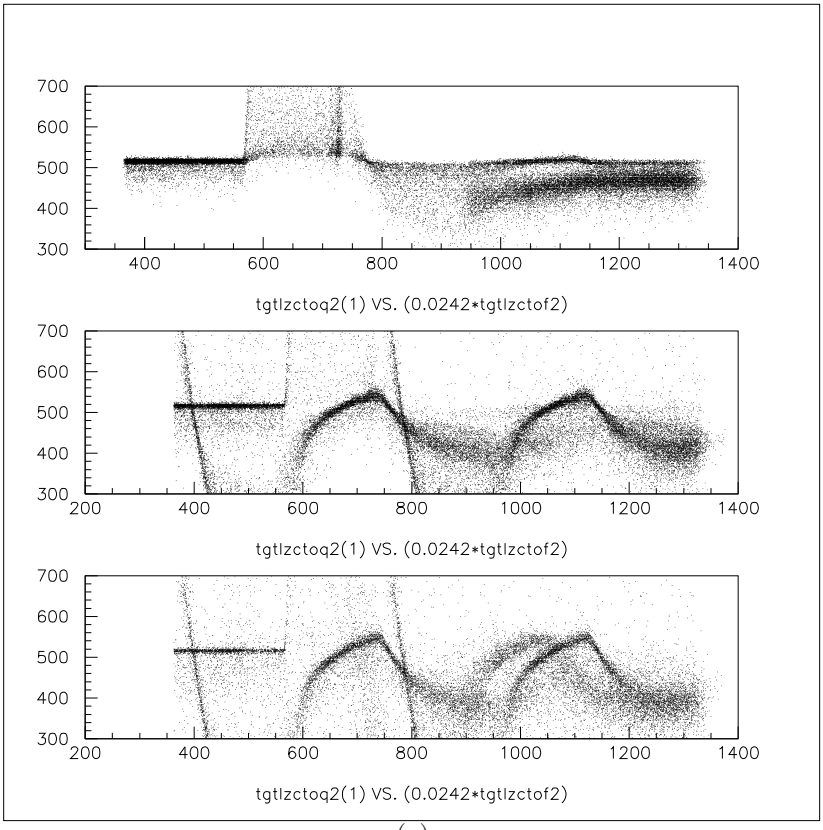

(a)

Figure 8: Scatterplots of QDC vs. PMT timing readout via multi-hit TDC. (Top). first TDC hit; (Middle). Second TDC hit; (Bottom).Third TDC hit.

In the top panel of this figure the scatterplot of QDC_2 vs. TDC_2 is shown in the region of QDC readout values around its pedestal (520 ch). According to this plot the QDC values are spread below the pedestal over the entire TDC scale except for the interval (570,770) ns, where the QDC values are significantly higher than the pedestal. This interval corresponds to coincidences of the PMT signal with the QDC gate, i.e. to the real events associated with electrons in the scintillator that coincide with the CLAS trigger. In the TDC scale, the QDC gate leading edge[14] corresponds to 770 ns, while its trailing edge is at 550 ns.

The narrow vertical strip at 550 ns is the manifestation of sub-nanosecond timing resolution of the CTOF-FM counter, relative to the CLAS trigger signal. This band is well fit into the QDC gate and we note that such scatterplots may be used to fit PMT signals into the QDC gate.

The rest of the events in this plot are accidental coincidences of the CLAS trigger with the hit in our counter. Usually such events have been ignored. However, they may inform us about the experimental environment.

[14]Real time runs from right to left on the TDC scale.

Let us consider the same scatterplots for the second and the third TDC hits shown in middle and bottom panels, respectively. There are very little statistics in the narrow band at 550 ns in the middle panel, and nothing in this area in the bottom panel. Almost all events are accidental coincidences with the CLAS trigger. We emphasize that the QDC value is the integral of the input current within the QDC gate (200 ns). Both panels clearly indicate the pickup with a period of 400 ns that looks in phase with the CLAS trigger timing.

We may verify this assumption. The trigger timing of CLAS includes the propagation time of the triggering particles. Therefore, it may be improved via propagation time corrections to the timing of the interaction at the vertex. Moreover, it may be further improved to the timing of the original electron bucket using the accelerator RF signal as the timing reference. The corresponding scatterplots after all the aforementioned corrections were applied are shown in Fig. 9.

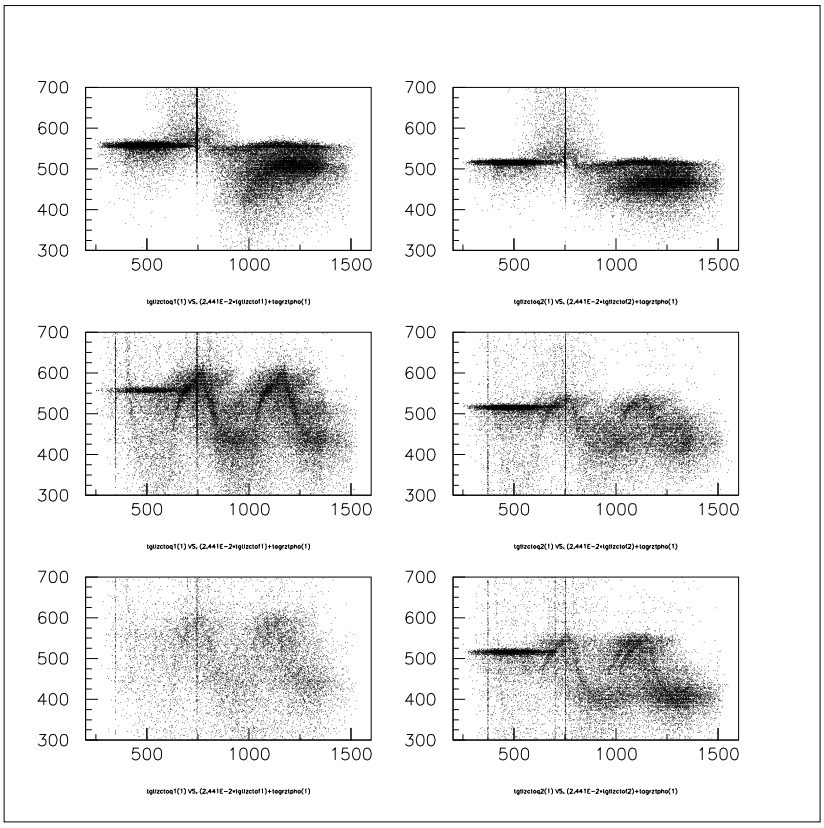

Figure 9: Timing of the first PMT (left panels) and the second PMT (right panels) of the CTOF-FM counter relative to the RF signal of the accelerator. Top, middle, and bottom panels are for the first, second, and third TDC hits, respectively. Horizontal scales (ns) are for the PMT timing. Vertical scales (counts) are for the QDC counts.

Very narrow strips at 750 ns show the sub-nanosecond timing resolution of our PMTs. There are several very narrow satellites in the middle and bottom panels. All the sub-nanosecond strips are much narrower than in Fig. 8a. However, the periodic pickup signals are spread in a wider region than in Fig. 8a obtained with reference to the CLAS trigger timing. Hence, we may conclude that the pickup is definitely not related to the accelerator

and, therefore, it is not a problem with the design of the CTOF-FM counter.

From further considerations of our beam measurements, we will see that this pickup may be the reason for a 30% worse TOF resolution compared to the bench tests. In order to achieve the optimal TOF results, the source of pickup in the DAQ system of CLAS should be localized and eliminated. However, firstly, it was not possible during the routine data taking, and secondly, it was not necessary, since the main goal of our tests was to compare two different PMTs in an identical environment. Hence, we continue our measurements, with this pickup as one of the environmental parameters, which cannot change the relative timing resolution of the fine-mesh and linear-focused PMTs.

A meaningful data set required several hours of data taking (one standard run of CLAS) at PMT counting rates of 0.6-0.7 MHz. After enough data were taken with the two R5924 PMTs, both PMTs were replaced with R2083 PMTs and we took enough data in this configuration.

In the following section we describe the results of the off-line analysis. We address the major parameters of a secondary electron hit, which are relevant to the TOF resolution of the CTOF-FM counter, and discuss all relevant plots.

5.2.2 Parameters of Electron Hit in the Scintillator

Energy deposition in the scintillators and PMT high voltage. The energy deposition of MIPs in the 3-cm-thick counter is about 6 MeV. Comparison of different PMT designs has to be performed at equal gains and number of primary photoelectrons. The high voltage of each PMT was varied to position the MIP peak at a QDC value of 1300. Thus we obtained raw QDC_1 and QDC_2 spectra for the two R5924 PMTs as shown in Fig. 10a. Similar spectra for the two R2083 PMTs are shown in Fig. 10b.

The maximas of all four spectra are located at about channel 1300, while the corresponding pedestals are near channel 540. Taking into account that the splitter feeds the QDCs with 20% of the PMT anode signal, we estimate the gains of all four PMTs to be about 2×10^6.

Comparing the peak widths in Figs. 10a and 10b, we notice that the QDC resolution of the R5924 is about two time worse than that of the R2083. This indicates significantly less stable gain of the fine-mesh PMT compared to the linear-focused PMTs. Perhaps, this may be attributed to the planar "tower" design of the fine-mesh PMTs.

Coordinates along the scintillator. The x_t-coordinate distributions (Eq.(21)) of deflected electrons across the scintillator, viewed by the R5924 and R2083 PMTs, are shown in Figs. 11a and 11b, respectively. Both distributions are about 10-12 cm wide (FWHM). However, the width of the beam spot measured with the two R5924 PMTs is about 20% worse than with the two R2083 PMTs. Since the secondary beam width unlikely was changed, this could indicate a worse timing resolution of the fine-mesh PMTs.

The x_q coordinate from Eq.(22) exhibits a similar effect. It is interesting to compare the x-coordinates obtained with two independent methods. A sample of the x_t vs. x_q scatterplot is shown in Fig. 12a. In this figure one can see a 10-cm wide (in both projections) peak in the center of the plot, which corresponds to a secondary beam of deflected electrons. There is also a narrow band that spans from -30 cm to +30 cm in both scales. This band should

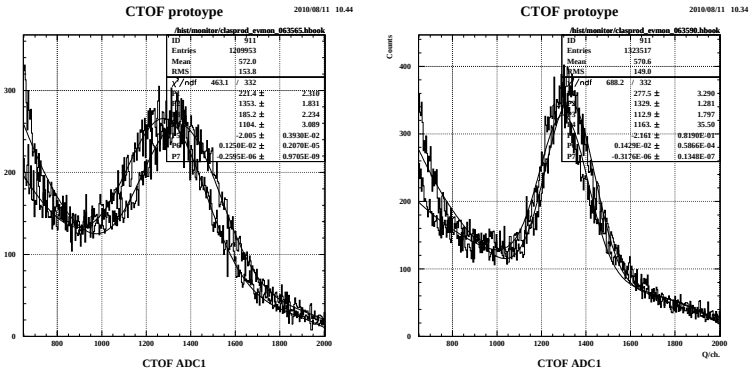

(a) (b)

Figure 10: Energy deposition of secondary electrons in the CTOF-FM counter instrumented with (a). Fine-mesh and (b). Linear-focused R2083 PMTs.

be attributed to secondary particles scattered in the material of the Tagger counters and mechanical framework.

This figure shows that both x-variables are properly calibrated. Here the effective speed of light was found to be 16 cm/ns, while the effective attenuation length of the scintillator is also reasonably close to the manufacturer's specifications of 3 m.

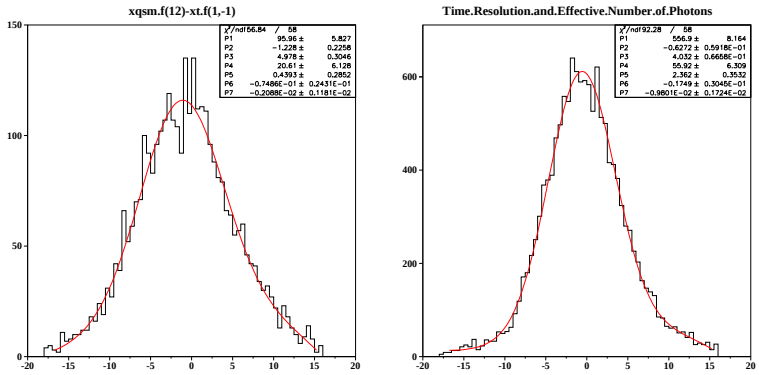

(a) (b)

Figure 11: (a). Secondary electron beam profile evaluated via QDC values. Counter instrumented with (a). Fine-mesh R5924 PMTs and (b) with linear-focused R2083 PMTs.

Number of primary photoelectrons We have estimated the number of primary photoelectrons N_{ppe} emitted from the photocathodes of each PMT using Eq.(34). The experimental values for the counter instrumented with the R5924 and R2083 PMTs are shown in Figs. 13a and 13b, respectively. The linear fit of the experimental dependencies results in the following number of primary photoelectrons generated by MIPs: 320 ± 50 for the R5924 and 240 ± 40 for the R2083 counter. Although the accuracy is not very good, these numbers are considered to be in agreement with our expectations. We have already mentioned that the light

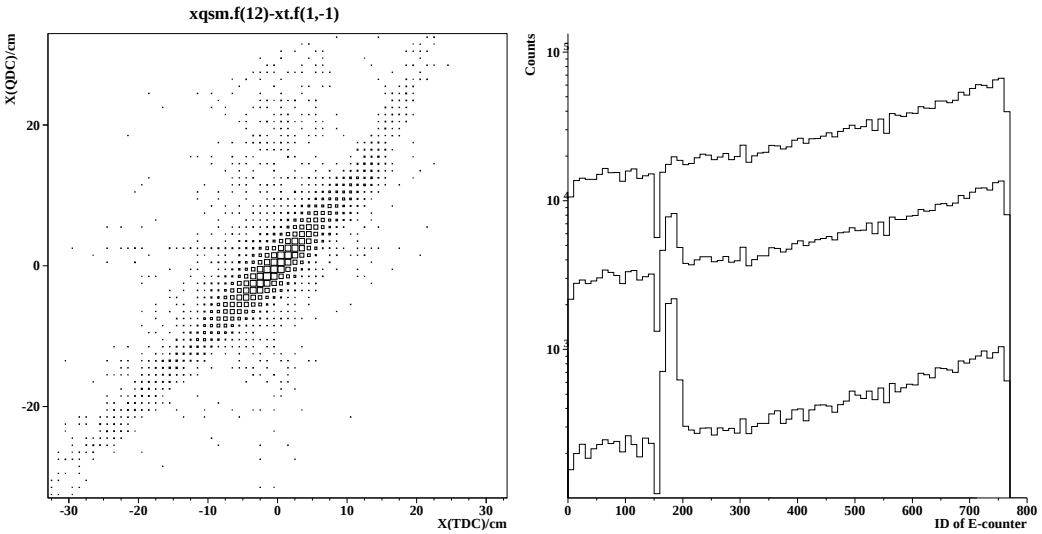

(a) (b)

Figure 12: (a). Scatterplot $x(q)$ vs. $x(t)$. (b). Tagger hodoscope profile (Tagger counter identification number) at different cuts.

guides were optimized for the R5924 PMT. Therefore, we expect the transmittance for the R2083 to be slightly worse. In addition, the magnetic field in the locations of the R2083 PMTs was about 3 G, a value that could reduce the effective number of photoelectrons. In combination all of this may explain the observed 1.3 ± 0.17 larger N_{ppe} obtained with the R5924 PMT.

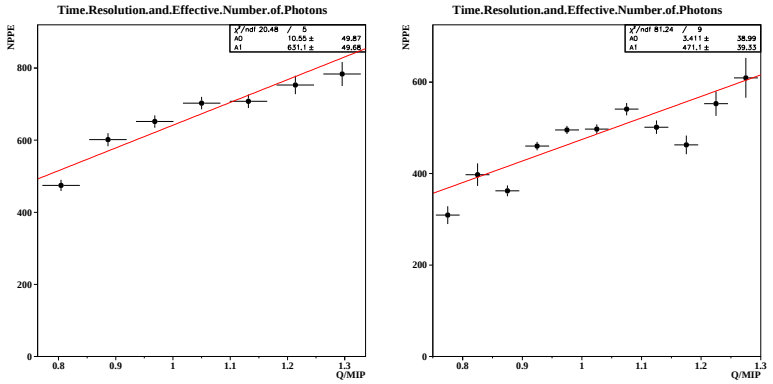

(a) (b)

Figure 13: Number of primary photoelectrons (N_{ppe}) at the photocathode of (a). Fine-mesh and (b). Linear-focused PMTs. N_{ppe} is shown as a function of the QDC value scaled in units of average QDC value for MIPs.

5.2.3 Selection Criteria for TOF Resolution Measurements

The selection criteria for the time resolution analysis were evaluated from the QDC distribution of both PMTs (Fig. 10), from the $x(t)$ plots (Fig. 11), and the $x(q)$ plot and the

Tagger counter identification number (T_{id}) plot (Fig. 12b). There are three plots in Fig. 12b that were obtained with different cuts. The most pronounced peak at T_{id} around 180 was obtained with the main cut that excluded the T_{id} requirement. The main cut used for the further evaluation of the TOF is defined as:

$$(-18 \leq x(t)/\mathrm{cm}, x(q)/\mathrm{cm} \leq 18)\ \&\ (0.8 \leq q_{1,2}/q_{MIP} \leq 1.4)\ \&\ (160 \leq T_{id} \leq 200). \qquad (35)$$

5.2.4 Time-Of-Flight Resolution

The time of flight for each hit in the CTOF-FM counter has been determined via Eq.(1). We require that the electron hits satisfy the criteria of Eq.(35). In Fig. 14a we show the TOF distribution of the deflected electrons obtained with the R5924 version of the CTOF-FM counter. One can see the peak in the center of this plot and two satellites located symmetrically. All peaks in this figure are separated by 2 ns intervals. This interval corresponds to the period of the accelerating RF. Therefore, the two satellite peaks may be attributed to the accidental coincidences of the CTOF-FM counts with the CLAS trigger. Hence, using the satellite peaks, the TOF scale may be calibrated to a stable 2-ns period of the accelerator radio frequency, and, from the Gaussian fit, we determine $\sigma_{R5924} = 153 \pm 5$ ps.

After several days of commissioning followed by a successful data taking period, both R5924 PMTs were replaced with R2083 PMTs. The TOF resolution data with the R2083 PMTs can be seen in Fig. 14b. All three peaks now look significantly narrower, and, according to the Gaussian fit, the TOF resolution of the R2083 counter is two times better, $\sigma_{R5924} = 86 \pm 3$ ps.

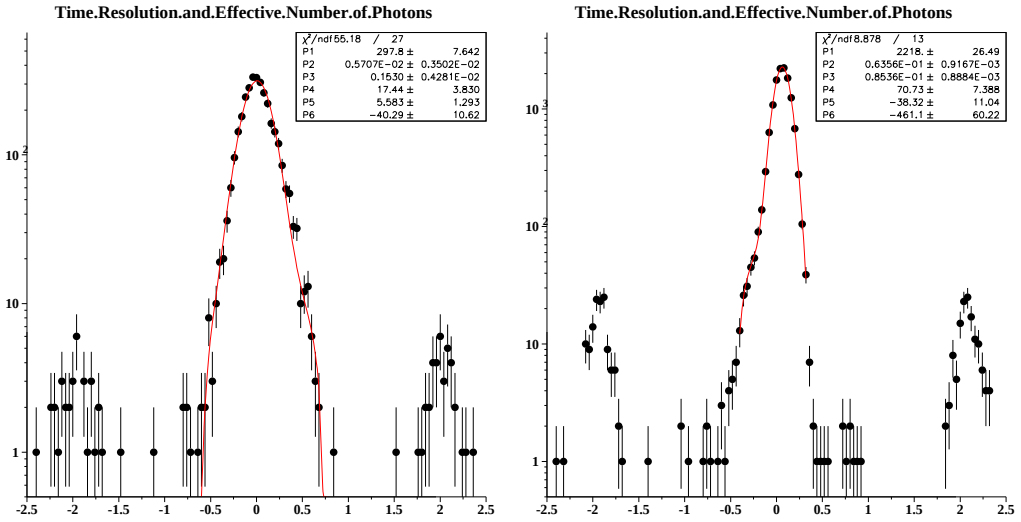

(a) (b)

Figure 14: Time-of-flight resolution of the CTOF-FM counter instrumented with (a). Fine-mesh R5924 and (b). Linear-focused R2083 PMTs.

We have summarized our TOF resolution measurements in Table 3. In the 1st and 2nd columns of this table the configuration of PMTs is listed. In the 3rd column the source of light radiation is specified, and in the 4th column the measured TOF resolutions are

shown. For both types of PMTs the beam resolution is 1.6 ± 0.1 times worse due to the aforementioned pickup problem. In the 5th column we list the ratio of the TOF resolution with the R5924 PMT to that obtained with the R2083 PMT in the same conditions. As seen from this column, the test-bench ratio and the beam ratio are in good agreement. In the last column the estimates for the TOF resolution are given under the assumption that the effects of pickup will be eliminated, i.e. the resolution obtained with the LED source will be reproduced in the beam measurements. The estimated value for the R2083 is the same as for the LED tests by definition, while the estimation for the R5924 counter manifests a very good agreement with the test bench result. In the last row the TOF resolution measured with the prototype triplet of baseline counters is listed.

PMT	Model	Source	σ_{TOF} /ps	σ_{PMT} $/\sigma_{R2083}$	Expected σ_{TOF}/ps	Ratio
1(left) 2(right)	R2083 R2083	LED	53±1	1		
1(left) 2(right)	R5924 R5924	LED	92±2	1.74±0.1		
1(left) 2(right)	R2083 R2083	beam	86±1	1	53 ± 1	1.62±0.05
1(left) 2(right)	R5924 R5924	beam	153±5	1.78±0.1	94 ± 4	1.62±0.12
6%CTOF triplet	R2083	cosmic	58±2	n/a	58 ± 1	1

Table 3: Summary table of TOF resolution measurements and estimates.

6 Summary and Outlook

Using an LED source we have performed comparative time resolution tests of R5924 (fine-mesh) and R2083 (linear-focused) PMTs. Here, both PMTs were illuminated with the same light flashes precisely split between the two photocathodes.

We have also measured the time-of-flight resolution of the final CTOF prototype with a secondary electron beam in Hall B. Here, two identical phototubes of different design were used with a double-sided readout of the same scintillator-light guide assembly.

In all of our tests the gain of each PMT was adjusted to the same value. The number of primary photoelectrons were measured simultaneously with the timing resolution. Thus, all of our comparative results are referenced to the same PMT gains and the same number of primary photoelectrons.

The resolution of the fine-mesh R5924 PMTs obtained with the LED light source was found to be about two times worse than with the R2083 PMTs. Beam tests also show that the TOF resolution of the counter instrumented with two R5924 is about two times worse than with the R2083 PMTs.

We note that the comparative tests of the two different PMTs were performed with identical light guides. In the real CTOF detector, the light guides for the linear-focused PMTs will be about two times longer. However, as can be seen from Table 2, the transmittance of a two times longer light guide for the R2083 will be only about 20% lower than for the R5924 PMTs. There are two major reasons for this relatively small difference. Firstly, the exponential dependence of the light guide transmittance upon its length. Provided that the effective attenuation length is about 2.5 m, we would expect 40% worse transmittance for the same PMT area. Secondly, the sensitive area of the R5924 PMT is only 12% larger than the luminous area of the scintillator. Moreover, it is 40% lower than the sensitive area of the R2083 PMT. Therefore the advantage of the shorter photon travel distances is compensated for by a larger number of surface reflections.

Taking into account all of these numbers, we conclude that the TOF resolution of the CTOF detector with R5924 PMTs will be about 50% worse than for our baseline design that, however, requires two times longer light guides and heavy magnetic shields.

We note that the main function of the CTOF detector in CLAS12 will be particle separation at the level of 3.3 σ. It is obvious that the Gaussian tails of the TOF distributions will result in particle misidentification. Following an exponential law, the background of foreign particles doubles for each additional 10% increase in TOF resolution. Therefore, although the linear-focused design requires magnetic shields, we cannot neglect the advantage of getting 50% better time resolution for a 35% lower price.

References

[1] V. Baturin *et al.*, CLAS-NOTE 2008-034, (2009)
http://www1.jlab.org/ul/Physics/Hall-B/clas/public/2008-034.pdf

[2] T. Massam, Guide-7, A general program for evaluating the properties of scintillation and Cherenkov counter optical systems, CERN Library (1976).

[3] F. Barbosa *et al.*, CLAS-Note 2006-011, (2006).
http://www1.jlab.org/ul/Physics/Hall-B/clas/public/2006-011.pdf

[4] Jefferson Laboratory Hall B CLAS12 Technical Design Report 2009.
http://www.jlab.org/Hall-B/clas12_tdr.pdf